JGR Planets

RESEARCH ARTICLE

10.1029/2023JE008181

Retrieval of Ar, N_2, O, and CO in the Martian Thermosphere Using Dayglow Limb Observations by EMM EMUS

J. S. Evans[1], J. Deighan[2], S. Jain[2], V. Veibell[1], J. Correira[1], H. Al Matroushi[3], H. Al Mazmi[4], M. Chaffin[2], S. Curry[2], N. El-Kork[5,6], S. England[7], F. Eparvier[2], M. Fillingim[8], G. Holsclaw[2], M. Khalil[9], R. Lillis[8], F. Lootah[3], S. Mahmoud[5], T. Plummer[2], E. Soto[1], J. Tennyson[10], E. Thiemann[2], and S. N. Yurchenko[10]

[1]Computational Physics, Inc., Springfield, VA, USA, [2]Laboratory for Atmospheric and Space Physics, University of Colorado, Boulder, CO, USA, [3]Mohammed Bin Rashid Space Center, Dubai, UAE, [4]United Arab Emirates Space Agency, Abu Dhabi, UAE, [5]Physics Department, Khalifa University, Abu Dhabi, UAE, [6]Space and Planetary Sciences Center, Khalifa University, Abu Dhabi, UAE, [7]Virginia Tech, Blacksburg, VA, USA, [8]Space Sciences Laboratory, University of California Berkeley, Berkeley, CA, USA, [9]Mechanical Engineering Department, Khalifa University, Abu Dhabi, UAE, [10]University College London, Physics and Astronomy, London, UK

Key Points:

- Remotely sensed CO densities retrieved from 130 to 160 km for the first time are ∼45% lower than MCD 6.1 predictions for similar conditions
- Mean retrieved Ar, N_2, and O densities from 130 to 160 km are lower than MCD 6.1 and NGIMS by 10%–15%, ∼75%, and 35%–45%, respectively
- High spectral resolution observations by EMM EMUS show the first detection of C I 119.3 nm emission blended with N I 120 nm emission

Supporting Information:

Supporting Information may be found in the online version of this article.

Correspondence to:

J. S. Evans,
evans@cpi.com

Citation:

Evans, J. S., Deighan, J., Jain, S., Veibell, V., Correira, J., Al Matroushi, H., et al. (2024). Retrieval of Ar, N_2, O, and CO in the Martian thermosphere using dayglow limb observations by EMM EMUS. *Journal of Geophysical Research: Planets*, *129*, e2023JE008181. https://doi.org/10.1029/2023JE008181

Received 3 NOV 2023
Accepted 25 MAR 2024

Abstract The Emirates Ultraviolet Spectrometer (EMUS) onboard the Emirates Mars Mission (EMM) Hope probe images Mars at wavelengths extending from approximately 100 to 170 nm. EMUS observations began in February 2021 and cover over a full Mars year. We report the first limb scan observations at Mars of ultraviolet emissions Ar I 106.6 nm, N I 120 nm, and carbon monoxide (CO) Fourth Positive Group ($A - X$) band system excited by electron impact on CO. We use EMUS limb scan observations to retrieve number density profiles of argon, molecular nitrogen, atomic oxygen, and CO in the upper atmosphere of Mars from 130 to 160 km. CO is a sensitive tracer of the thermal profile and winds in Mars' middle atmosphere and the chemistry that balances CO_2 in the atmosphere of Mars. EMUS insertion orbit special observations demonstrate that far ultraviolet limb measurements of the Martian thermosphere can be spectroscopically analyzed with a robust retrieval algorithm to further quantify variations of CO composition in the Martian upper atmosphere.

Plain Language Summary This study focuses on satellite observations of ultraviolet light by the Emirates Mars Ultraviolet Spectrometer onboard the Emirates Mars Mission. The observed ultraviolet light is generated by argon, oxygen, nitrogen, and carbon monoxide and is used to determine the abundance of these gases in the upper atmosphere of Mars (130–160 km). We present the first remotely sensed measurements of argon and carbon monoxide abundances in the upper atmosphere of Mars. Mean retrieved argon, nitrogen, and oxygen densities, respectively, are lower than general circulation model predictions and other direct measurements by 10%–15%, ∼75%, and 35%–55%. Carbon monoxide densities measured for the first time agree qualitatively with measurements by other instruments and model predictions for similar conditions. We demonstrate that ultraviolet observations can be analyzed with a robust technique to further quantify variations of carbon monoxide abundance in the Martian upper atmosphere.

1. Introduction

Over a time frame spanning more than four decades, ultraviolet (UV) emissions have been used to infer atmospheric composition and temperature of the upper atmosphere of Mars. All previous UV airglow limb scan observations at Mars were made at wavelengths longer than 110 nm. The Martian UV airglow was first observed by the Mariner 6 and 7 missions (>110 nm; resolution 1 nm) in 1969 followed by Mariner 9 (>110 nm, resolution 1.5 nm) in 1971–1972 (Barth et al., 1969, 1971, 1972; Stewart, 1972; Stewart et al., 1972; Strickland et al., 1972, 1973). More recently, observations by the Spectroscopy for the Investigation of the Characteristics of the Atmosphere of Mars (SPICAM) spectrometer on board Mars Express (>118 nm, resolution 0.8 nm) led to the discovery of emission due to solar energetic particles (Bertaux et al., 2005a; Brain et al., 2006; Dubinin et al., 2009; Ip, 2012; Leblanc et al., 2006, 2008) and chemiluminescence (Bertaux et al., 2005b, 2005c; Cox et al., 2008). Subsequent, more detailed analyses have been used to infer the global distribution of total ozone on Mars (Perrier et al., 2006).

Significant advances in our understanding of the atmospheric state of Mars have been enabled by NASA's Mars Atmosphere and Volatile EvolutioN (MAVEN) spacecraft, which arrived at Mars September 2014. The primary

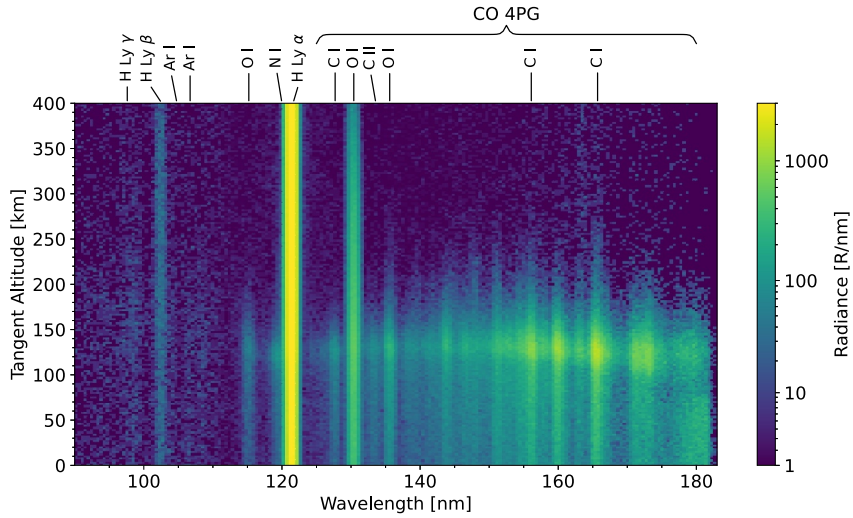

Figure 1. Spectrogram showing unbinned HR slit data taken during insertion orbit observation by EMUS on 25 February 2021 (L_s = 8.7°). The motion of the instrument slit is from top to bottom. At the peak of the emission layer (~130 km) the solar zenith angle is ~34°, latitude ~19°N, and local time ~14 hr. Prominent emission features and the spectral range of the CO 4PG band system are identified at the top of the figure.

objective of the MAVEN mission is to determine the present and historical rates of escape of the Martian atmosphere (Jakosky et al., 2015) by quantifying the diurnal, latitudinal, seasonal, and solar activity variations in the Martian atmosphere. Specifically, the Imaging Ultraviolet Spectrograph (IUVS; >110 nm, resolution 0.6 nm for the far ultraviolet detector; McClintock et al., 2015) and the Neutral Gas and Ion Mass Spectrometer (NGIMS; Mahaffy et al., 2015) onboard the MAVEN mission have characterized the composition and temperature of the Martian upper atmosphere as a function of latitude, longitude, local time, season, dust activity, and solar activity during a period spanning more than four Mars years (e.g., Jain et al., 2015, 2020; Mahaffy et al., 2015; Stevens et al., 2017). MAVEN IUVS limb scan observations have been used to retrieve altitude profiles of CO_2, N_2, and O densities covering Mars Years (MY) 32–37 (Evans et al., 2015, 2023a; Stevens, Evans, Lumpe, et al., 2015; Stevens, Evans, Schneider, et al., 2015).

In this study, we present retrievals of argon (Ar), molecular nitrogen (N_2), atomic oxygen (O), and carbon monoxide (CO) vertical density profiles in the Martian thermosphere from UV dayglow observations at Mars. We use special insertion orbit limb profiles from approximately 100 to 200 km tangent altitude by the Emirates Ultraviolet Spectrometer (EMUS) (Holsclaw et al., 2021) onboard the Emirates Mars Mission (EMM) Hope probe (Al Matroushi et al., 2021; Amiri et al., 2022). We first discuss EMUS limb scan observations followed by a discussion of the forward model and optimal estimation techniques used herein. We then present the methodology used for retrieval of Ar, N_2, O, and CO densities. We also compare our retrieved densities with measurements by other instruments currently orbiting Mars. In the final section, we summarize the most significant results of this study.

2. EMUS Observations

The nominal orbit of the EMM Hope probe has an apoapsis at 42,650 km and periapsis at 19,970 km with a 54.5 hr period. This high altitude orbit affords a synoptic view of Mars with near–total latitude–local time coverage every 9–10 days (Holsclaw et al., 2021). EMUS' high resolution (HR) and very high resolution (VHR) slits have angular widths of 0.18° and 0.05° and spectral resolutions of 1.3 and 0.4 nm (central 1°, 130–160 nm), respectively (Holsclaw et al., 2021). These are therefore the highest resolution UV spectra to date from the Mars limb. We also note that the signal-to-noise ratio (SNR) of the EMUS HR observations is ~4 times higher than MAVEN IUVS observations when binned to equivalent spectral and spatial resolutions (the EMUS HR SNR is ~2 times higher than VHR). For the observations presented herein (see Figure 1), EMUS remotely sensed the thermosphere from below 100 km to above 400 km tangent altitude, observing UV emissions (~100–170 nm) from hydrogen (H I 121.6 nm), molecular nitrogen (N I 120 nm and N_2 Lyman-Birge-Hopfield (LBH) bands), oxygen (O I 115.2 nm, 130.4 nm, and 135.6 nm), and carbon monoxide (CO Hopfield-Birge $B - X$, $C - X$, and

Table 1
Tangent Point Parameters for the EMUS Insertion Orbit Special Observations

Date	UT (hr)	Ls (deg)	Lat (deg)	Lon (deg)	SZA (deg)	LT (hr)	Slit
2021-02-25	01:59	8.68	18.83	40.08	33.96	14.07	HR
2021-02-26	11:36	9.36	18.66	268.76	33.87	14.08	VHR
2021-03-01	06:55	10.72	18.29	5.55	33.24	14.07	HR
2021-03-02	16:34	11.39	18.12	234.16	33.13	14.07	VHR
2021-03-05	11:53	12.74	17.75	330.99	32.51	14.05	HR
2021-03-06	21:32	13.42	17.60	199.51	32.31	14.05	VHR
2021-03-08	07:11	14.09	17.41	67.87	31.96	14.04	HR
2021-03-09	16:51	14.76	17.24	296.46	31.84	14.04	VHR

$E - X$, and Fourth Positive Group (4PG) $A - X$). The first data release, covering 10 February 2021 to 23 May 2021, was delivered in early October 2021 (see Data Availability Statement).

While EMUS has typically viewed in the nadir during normal operations, for the present analysis we utilize EMUS special insertion orbit limb scan profiles (i.e., when EMM transitioned to its nominal science orbit). The special observations were designed such that periapsis was low enough (~1,060 km) to permit remote sensing limb scans. The observations were repeated during eight orbits spanning 25 February 2021 to 9 March 2021, with four orbits using the 1.3 nm (HR) slit alternating with four orbits using the 0.4 nm (VHR) slit. Conditions for the eight observations are provided in Table 1.

The orientation of the slit during the insertion orbit special observations was approximately tangent to the surface (see Figure 1 in Chaffin et al., 2022). This enables us to increase the SNR of the observations by summing spectra corresponding to 20 spatial pixels along the slit situated about the center (i.e., horizontally). We also summed spectra in groups of three integration periods (i.e., vertically) to further boost the SNR. As shown in the Figure S1 in Supporting Information S1, the HR and VHR spectral resolutions vary along the slit, thus the resolution of the binned data are 1.36 and 0.82 nm, respectively. Accounting for a 0.7 km spread in altitude sampling due to planet curvature for the 20 spatial bins near the middle of the slit, the range from the highest to lowest tangent altitudes that fall into the slit across 3 integrations near 130 km is 8.2 km for the VHR and 14.4 km for the HR slit.

The summed spectra were then input to a multiple linear regression (MLR) routine to fit the spectra using model templates that are run through an instrument model to simulate the slit-dependent point spread function (PSF) of the instrument (Carnall, 2017; Jain et al., 2015; Stevens, Evans, Lumpe, et al., 2015; Stevens, Evans, Schneider, et al., 2015; Virtanen et al., 2020). The instrument model convolves the model templates with a PSF derived as the combination of a Moffat PSF and a Gaussian PSF. The parameters determining the PSF shape are optimized through least squares regression against a Lyman α spectrum (near 121.6 nm) from the center of the detector. Each model template is then shifted in wavelength with a flux-preserving rebinning procedure based on a cross correlation between the template and a sample MLR residual after having subtracted all other fit sources from the observation. This process accounts for small amounts of dispersion (less than 1 Å) across the detector and is treated as constant along the spatial and integration dimensions, as well as from scan to scan. The shifts are determined from VHR data and are used for both HR and VHR data. This process is repeated with a new MLR fit using templates shifted by the initially determined values to get a final set of wavelength offsets. A more detailed description of the fitting methodology is provided in the Supporting Information S1.

3. Spectral Analysis

In this study, we use EMUS dayglow limb observations of Ar I 106.6 nm, N I 120 nm, O I 135.6 nm, and CO 4PG ($A - X$) to retrieve vertical density profiles from 130 to 160 km of Ar, N_2, O, and CO, respectively, using the Atmospheric Ultraviolet Radiance Integrated Code (AURIC; Strickland et al., 1999). The AURIC software package was developed for upper atmospheric radiance modeling from 80 to 1,000 nm. AURIC has been used to study the dayglow from the Earth (Bishop et al., 2007), Titan (Stevens, Evans, Lumpe, et al., 2015; Stevens, Evans, Schneider, et al., 2015; Strobel et al., 1991, 1992), Triton (Strobel et al., 1991), and Pluto (Schindhelm

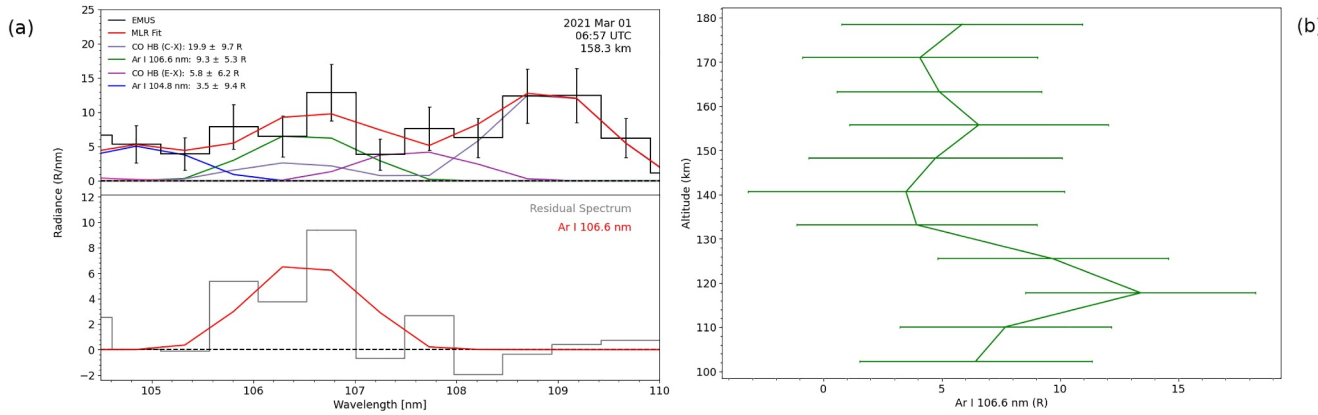

Figure 2. (a) Top: EMUS observation using the HR slit on 1 March 2021. The corresponding tangent altitude of the observation is provided in the upper right. The legend indicates the relative contribution of each component source used in the multiple linear regression (MLR) fit as determined by integrating the spectra within the fitting region. The wavelength range used to fit the data is as shown in the figure. There is no background subtraction for the spectral radiances in the Level 2A files, thus the background is removed by the MLR data reduction. Bottom: Residual spectrum comparing the MLR fit to the observation after subtracting from the observation all MLR sources except the one selected for analysis. (b) Altitude profile of Ar I 106.6 nm emission obtained by performing MLR fits of spectra for each tangent altitude.

et al., 2015; Steffl et al., 2020). Application of the AURIC model to the Martian dayglow is described by Evans et al. (2015), Stevens, Evans, Lumpe, et al. (2015), and Peterson et al. (2016).

3.1. Argon 106.6 nm Singlet

Argon emission at 104.8 nm $\left(3p^6\ {}^1S_0 \rightarrow 3p^5\left({}^2P_{\frac{1}{2}}\right)4s\left[\frac{1}{2}\right]_1\right)$ and 106.6 nm $(3p^6\ {}^1S_0 \rightarrow 3p^5\left({}^2P_{1\frac{1}{2}}\right)4s\left[1\frac{1}{2}\right]_1$; no other branches) was detected by Feldman et al. (2000) in the Hopkins Ultraviolet Telescope (HUT) disk-averaged spectrum of Mars. While the fluorescence efficiency of the 104.8 nm line is 3.5 times higher than for the 106.6 nm line, the 106.6 nm line was found to be brighter than 104.8 nm. Feldman et al. concluded that this was due to the higher CO_2 absorption cross section at 104.8 nm. Using a CO_2 absorption cross section of 1.28×10^{-17} cm^2 (Huestis & Berkowitz, 2011), we estimate the opacity at 106.6 nm to be near unity for a tangent altitude of 130 km increasing to about 20 at 110 km. We utilize EMUS observations of the brighter 106.6 nm line for retrieving altitude profiles of Ar density.

MLR results for the Ar I 106.6 singlet are shown in Figure 2. The top plot of panel (a) on the left illustrates an observation using the HR observation slit on 1 March 2021. The spectrum shown in panel (a) corresponds to the tangent altitude provided in the upper right. The legend indicates the relative contribution of each component source used in the MLR fit as determined by integrating the spectra within the fitting region. The uncertainty for each integrated source is calculated by taking the reported profile uncertainty and scaling it by the relative amount of the source template contained within the fitting region (i.e., source templates for molecular features may extend outside of the fitting region because the templates include all allowed rovibrational transitions). The bottom plot of panel (a) shows the residual spectrum comparing the MLR fit to the observation after subtracting from the observation all MLR sources except the one selected for analysis. Panel (b) on the right shows the altitude profile of Ar I 106.6 nm emission obtained by performing MLR fits of spectra for each tangent altitude.

Since the CO $C-X$ (0,0) band at 108.8 nm blends with Ar I 106.6 nm in the HR slit observations, a corresponding component source template is included when performing the MLR fit to retrieve Ar I 106.6 nm intensities. Although the CO $C-X$ (1,0) band at 106.3 nm was not detected by Feldman et al. (2000) or Krasnopolsky and Feldman (2002), we estimate that the band intensity may constitute up to 25% of the total intensity of the feature at 106.6 nm (see Section 6). Thus, our source template for CO $C-X$ includes both the (0,0) and the (1,0) bands. Details of the CO $C-X$ band model are provided in Appendix A. Similarly, the CO $E-X$ (0,0) band at 107.6 nm was detected by Krasnopolsky and Feldman (2002) and is evident in the EMUS HR observation shown in Figure 2, so we include a corresponding component source template for this band in the MLR fits. Details of the CO $E-X$ band model are also provided in Appendix A. As evident in Figure 2a, the rotational structure in the CO $C-X$ and $E-X$ band models (Figures A2 and A3) is not resolvable by EMUS using either HR or VHR slit. The much weaker CO $E-X$ (1,0) band near 105.3 nm was not detected by Krasnopolsky and Feldman (2002) and was

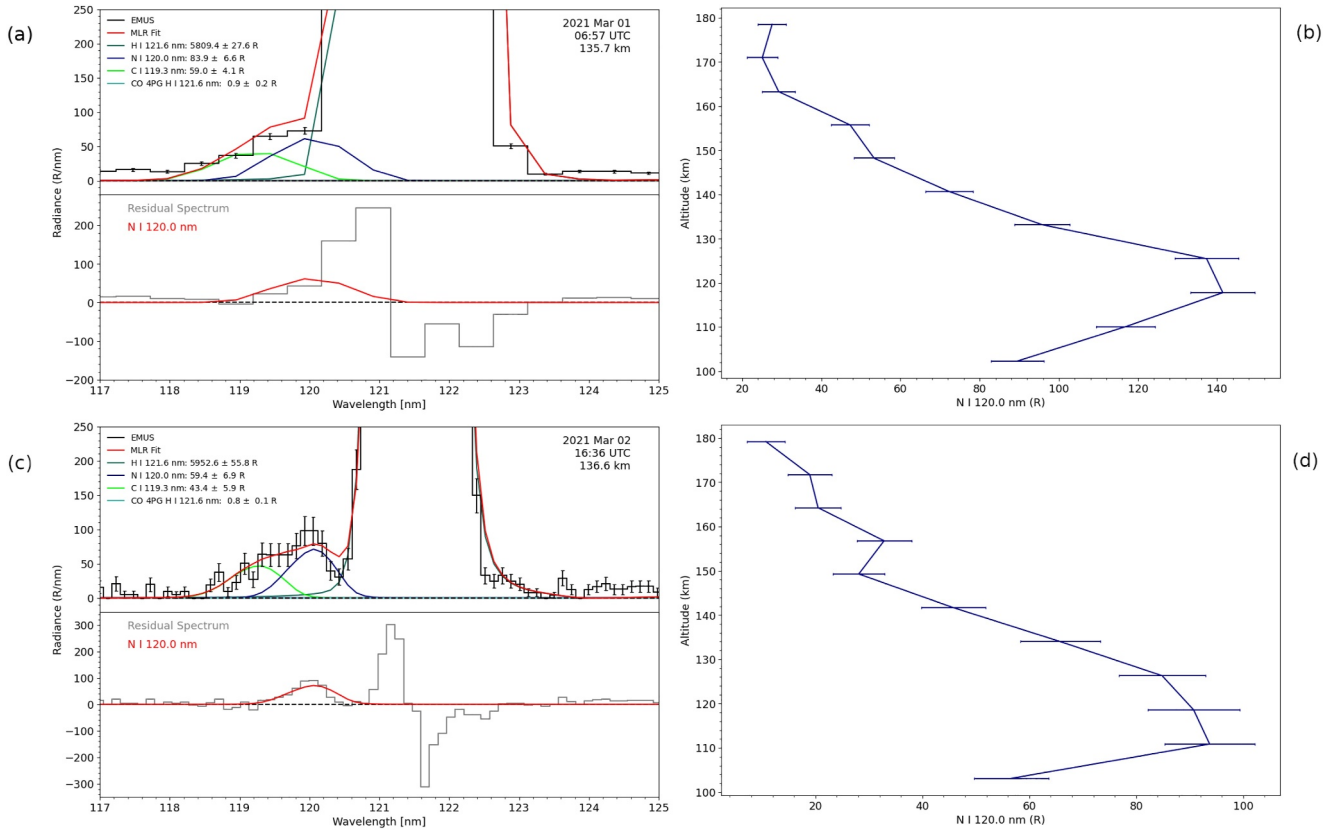

Figure 3. (a, b) Same as Figure 2 but for N I 120.0 nm triplet. (c, d) Same as panel (a, b) but for the very high resolution observation on 2 March 2021. The wavelength range used to fit the data is as shown in the figure. The spectral structure in panels (a, c) (bottom) near Lyman α is due to small uncertainties in the wavelength fitting and the large relative brightness of the Lyman α feature.

too weak to be detected in the laboratory by Tilford et al. (1965). Since this very weak band lies at the far blue edge of the feature at 106.6 nm in the HR observations, we do not include a component source template for this band in our MLR fits.

The sources of Ar 106.6 nm emission include electron impact excitation of Ar and resonance scattering of solar photons. For the electron impact source we use the cross section of Tsurubuchi et al. (1996). We estimate that ~70% of the column emission rate on the limb results from photoelectron impact on atomic argon. The resonance scattering source is calculated using the REDISTER code (Gladstone, 1982) with a solar flux at Mars of 1.5×10^7 (photons cm^{-2} s^{-1}) and a CO_2 absorption cross section of 1.28×10^{-17} cm^2 (Huestis & Berkowitz, 2011). It is worth mentioning that Feldman et al. (2000) and Krasnopolsky and Feldman (2002) ignored multiple scattering and photoelectron impact excitation in their analyses. However, Lootah et al. (2022) concluded that the Ar I 106.6 nm emission is optically thick to self-absorption in the Martian thermosphere.

3.2. Nitrogen 120 nm Triplet

The N I 120 nm triplet was identified in the spectrum of Mars for the first time by Feldman et al. (2000). Though the emission feature is blended with the much brighter H I Lyman α line at 121.6 nm, they were able to estimate a disk integrated brightness of ~12 R for near solar minimum conditions. As evident in Figure 3, EMUS observations indicate that the N I 120 nm feature is blended with a nearby feature on the blue side that was not detected by Feldman et al. (2000). We identify this source of emission to be the C I 119.3 nm multiplet, which was observed in the laboratory by Ajello et al. (2019) and is produced by electron impact on CO and CO_2 (and possibly other sources). This feature is included in MLR fits to EMUS observations in order to isolate the N I 120 nm emission.

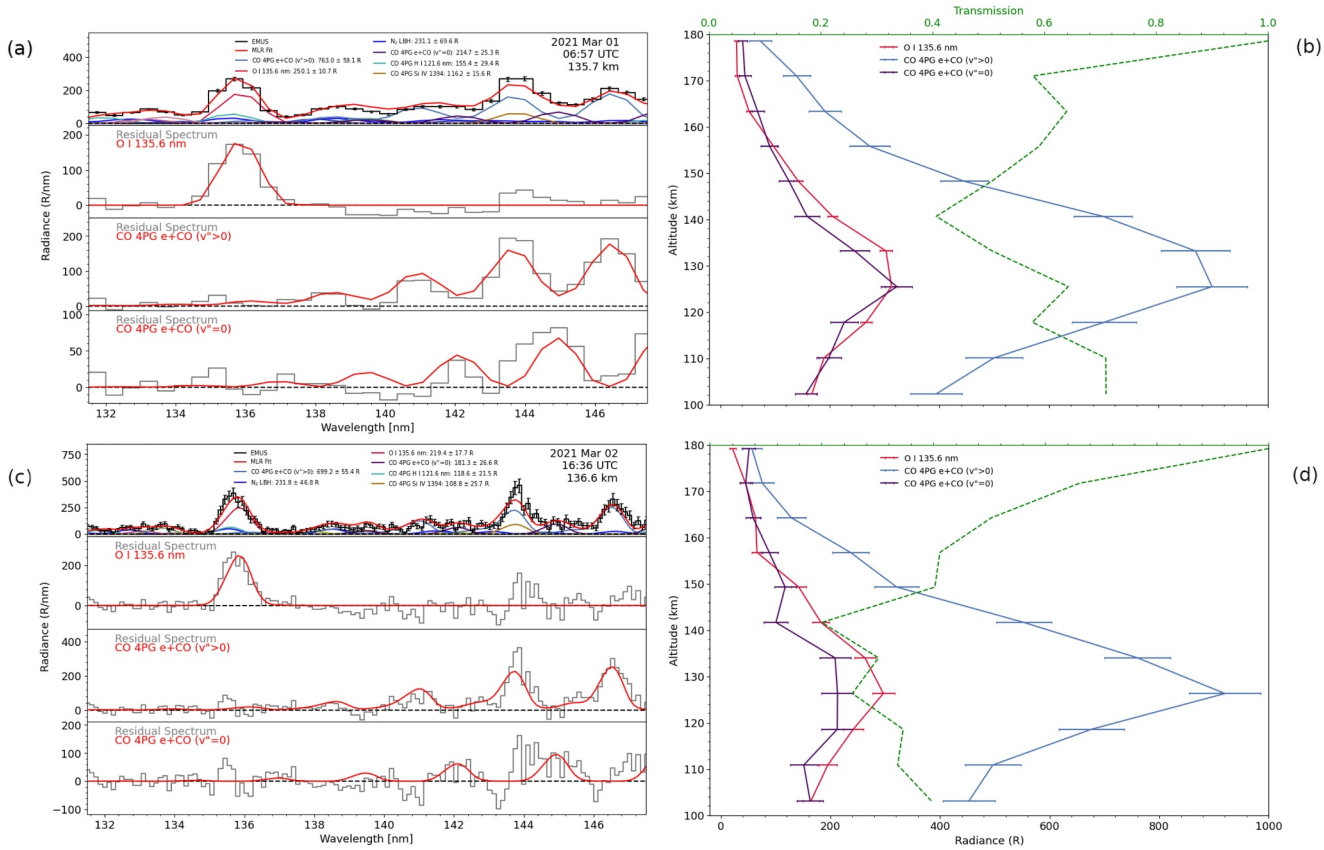

Figure 4. Same as Figure 3 but for blended O I 135.6 nm doublet and e + CO 4PG ($A - X$) band system. The wavelength range used to fit the data is as shown in the figure. The dashed line in panels (b, d) estimates the transmission (i.e., opacity) of e + CO 4PG emission and is obtained by normalizing the ratio of optically thick ($\nu'' = 0$) and optically thin 4PG emission ($\nu'' > 0$) to unity at the highest tangent altitude shown in the figure.

The primary source of N I 120 nm emission is from photodissociative excitation of N_2. For this source, we use the cross section and detailed modeling approach described by Bishop and Feldman (2003). Although electron impact dissociative excitation of N_2 is a relatively weak source of N I 120 nm emission, we include this source in our forward model using the cross section measured by Ajello and Shemansky (1985). We also include the weak source from electron impact on atomic nitrogen using the solar minimum atomic nitrogen density from Fox and Hać (2018) and the renormalized cross section from E. Stone and Zipf (1973) reduced by 40%, as suggested by Bishop and Feldman (2003).

Since N I 120 nm triplet emission involves a dipole allowed transition with the ground state, radiative transport (multiple scattering and self-absorption) must be taken into account (Bishop & Feldman, 2003). For radiative transport modeling we use the REDISTER code (Gladstone, 1982) with the optical parameters provided in Figure 4 from Bishop and Feldman (2003); following these authors, we also ignore solar resonance scattering.

3.3. Oxygen 135.6 nm Doublet

The emission feature at 135.6 nm seen in the left panels of Figure 4 is a blend of the O I 135.6 nm doublet, the CO 4PG (14,4) band excited by solar Lyman α photons, and a weak contribution from the N_2 LBH (3,0) band (Durrance, 1981; Kassal, 1975, 1976). Feldman et al. (2000) concluded that most of the observed emission at 135.6 nm is due to CO based on full disk observations of Mars using the Astro-2 observatory on HUT. The component source template used by the MLR fitting technique for the CO 4PG (14,4) spectrum is the same as reported by Evans et al. (2022) whereas the N_2 LBH template is described by Budzien et al. (1994). The templates used for CO 4PG produced by electron impact on CO are discussed in the next section.

The atomic oxygen doublet at 135.6 nm arises from the transition $O(^5S_o^2) \rightarrow O(^3P_{1,2})\,h\nu$ (135.56, 135.85 nm). The sources of emission include electron impact dissociative excitation of CO_2 as well as electron impact excitation of O, which is the dominant source (Fox & Dalgarno, 1979; Simon et al., 2009). Resonance scattering of solar photons is not an important source since the transition to the ground state is spin forbidden (Fox, 1992). Photodissociation of CO_2 and electron impact dissociation of O_2 are also negligible sources and are ignored. To calculate the emission rate for electron impact on O we use the cross section of Meier (1991). For electron impact dissociation of CO_2 we use the cross section of Ajello (1971) normalized to the revised cross section at 100 eV measured by Ajello et al. (2019). For energies above 300 eV we use the cross section of Jackman et al. (1977) normalized to the Ajello et al. (2019) cross section at 100 eV. For radiative transport modeling we use the REDISTER code (Gladstone, 1982) with the optical parameters provided by Meier (1991). Using CO_2 absorption cross sections of 7.5×10^{-19} and 5.7×10^{-19} cm^2 (195 K; Venot et al., 2018), respectively, the optical depth at 130.4 and 135.6 nm is about unity for a tangent altitude of 125 km increasing to ~10 for a tangent altitude of 110 km. We estimate the line center self-absorption optical depth at 125 km tangent altitude to be $\sim 10^4$ for O I 130.4 nm and about unity for O I 135.6 nm.

3.4. CO 4PG $A - X$

The CO 4PG bands ($A\ ^1\Pi - X\ ^1\Sigma^+$) were identified in the HUT spectrum of Mars by Feldman et al. (2000). The sources of production of the CO 4PG bands are photodissociative and electron impact excitation of CO_2, dissociative recombination of CO_2^+, direct electron impact of CO, and resonance fluorescence of solar ultraviolet radiation (Durrance, 1981; Fox & Dalgarno, 1979). The wavelength range used to perform MLR fits of O I 135.6 nm, shown in Figure 4 and discussed in the previous section, extends from 131.5 to 147.5 nm to account for minor contributions near 135.6 nm from CO 4PG emission produced by electron impact on CO. This source of CO 4PG emission is brighter than resonance fluorescence of solar ultraviolet radiation (e.g., CO 4PG (14,4) band excited by solar Lyman α photons) and provides sufficiently high SNR to retrieve CO densities. The electron impact CO 4PG component source templates used for the MLR fits are based on the optically thick band model described by Ajello et al. (2019). As done when fitting laboratory measurements, we account for optical thickness (i.e., CO self absorption) effects in the EMUS observations by separating the CO 4PG band system into optically thick bands that terminate in the ground state ($\nu'' = 0$) and optically thin bands ($\nu'' > 0$), both with a rotational temperature of 200 K.

4. Density Retrieval Algorithm

We infer atmospheric composition from EMUS insertion orbit limb scan profiles using the Generalized Retrieval and ANalysis Tool (GRANT). This tool merges AURIC with OPTimal estimation (hereafter OPT) retrieval algorithms (Lumpe et al., 1997, 2002, 2007). The GRANT tool has been applied to dayglow observations of Titan for the retrieval of N_2 and methane (Stevens, Evans, Lumpe, et al., 2015) and Mars for the retrieval of CO_2, N_2, and O (Evans et al., 2015; Stevens, Evans, Schneider, et al., 2015). For the present study, we use the Mars algorithm in order to retrieve Ar, N_2, O, and CO densities using EMM EMUS limb scan observations of Ar I 106.6 nm, N I 120 nm, O I 135.6 nm, and CO 4PG ($A - X$) emission, respectively. Our forward model calculations assume that the atmosphere is spherically symmetric along the line of sight, which is reasonable for the solar zenith angles considered here (32°–34°). Details of the optimal estimation formalism are provided by Evans et al. (2015, 2023a).

An a priori covariance matrix is used to characterize the uncertainty in the a priori estimate of the state vector and provides smoothing constraints in the retrievals. In practice, it is adjusted to optimize the trade-off between noise suppression and information content from the data. In this study, the a priori covariance varies with altitude in the following manner:

$$\sigma_{ij}^2 = \begin{cases} [0.5\, x_{a_i}]^2 & i = j \\ \sigma_{ii}\, \sigma_{jj} \exp\left[-((z_i - z_j)/H)^2\right] & i \neq j \end{cases} \quad (1)$$

where i and j are altitude indices, z_i is the ith altitude, x_{a_i} is the a priori density at altitude z_i, $H_i = kT_i/mg_i$ is a length scale (i.e., scale height) that determines the degree of vertical coupling along the rows of the covariance matrix, k

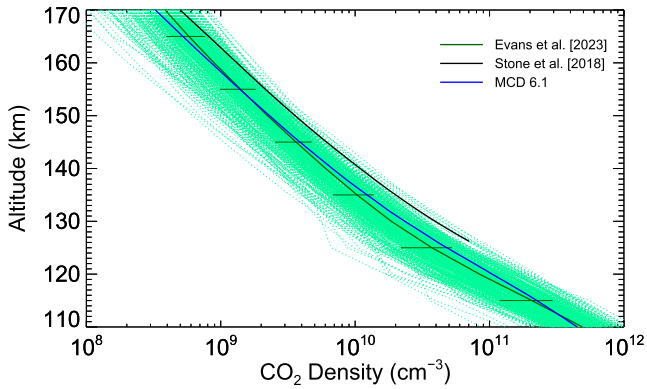

Figure 5. Mean MCD 6.1 CO_2 density profile used for the a priori atmosphere for the EMUS retrievals (blue; solar min; low dust activity; L_s = 10°; lat = 15°N; lon = same as EMUS observations in Table 1) compared to mean Deep Dip 8 profile from S. W. Stone et al. (2018) (black; L_s = 76.3°; LT = 13.7 hr; latitude = 18.9°N; SZA = 25°; mean uncertainty ~25%) and mean profile retrieved from MAVEN IUVS observations of O I 297.2 nm emission from Evans et al. (2023a) (green). The horizontal bars represent 1-σ natural variability. The individual CO_2 profiles from Evans et al. (2023a) for the time frame of the EMUS observations are shown in light green (lat = 20°–60°, primarily southern hemisphere; SZA = 20°–85°).

is Boltzmann's constant, T_i is the temperature at z_i, m is the molecular mass, and g_i is the gravitational acceleration at z_i.

The diagonal elements in Equation 1 weight the data with altitude in order to facilitate convergence, where the weighting is determined from simulations of the airglow data between 80 and 200 km. The a priori atmosphere (CO_2, Ar, N_2, O, CO) used to initiate the density retrievals consists of mean densities as a function of altitude from the Mars Climate Database version 6.1 (MCD; Millour et al., 2018) corresponding to the time frame and conditions of the EMUS observations (low solar and dust activity). Since the spectral features in the EMUS observations do not provide a direct measure of the CO_2 density, we use the mean MCD 6.1 CO_2 density profile for our density retrievals.

In situ measurements of abundances of CO_2, Ar, O, N_2, and CO have been made by NGIMS on the MAVEN satellite. These measurements are collected from ~500 km to as low as 125 km during low-altitude MAVEN "Deep Dip" orbits (Bougher et al., 2015). Figure 5 shows the mean MCD 6.1 CO_2 density profile (blue) compared to the mean Deep Dip 8 NGIMS profile from S. W. Stone et al. (2018) (black) and the mean profile retrieved from MAVEN IUVS observations of O I 297.2 nm emission from Evans et al. (2023a) for the time frame of the EMUS observations (dark green). The latitudes of the IUVS observations range from 20° to 60° and are predominantly in the southern hemisphere. The SZA values range from 20° to 85°. The latitude and SZA of the EMUS observations are ~17–19°N and ~33°, respectively. The mean MCD 6.1 CO_2 profile agrees with the mean profile from Evans et al. (2023a) within 1-σ natural variability whereas the mean Deep Dip 8 NGIMS CO_2 profile from S. W. Stone et al. (2018) is systematically higher by ~60%. The mean uncertainty of the NGIMS CO_2 density (130–160 km) is ~25% (S. W. Stone et al., 2018).

5. Results

The procedure used in this analysis sequentially retrieves Ar, N_2, O, and CO density profiles by fitting EMUS limb scan observations using an optimal estimation algorithm. The density retrievals use a total of 26 parameters for each limb scan: constituent densities on a fixed altitude grid (25 grid points) and a forward model brightness scale factor. The retrieval altitude grid uses equally spaced increments of 10 km from 80 to 120 km, 5 km from 120 to 170 km, and exponentially increasing increments up to 600 km (note that the observation tangent altitude grid and the retrieval vertical altitude grid are not directly coupled within the retrieval algorithm). We perform Ar retrievals first, since it is inert with very low chemical reactivity (Ott, 1991), followed sequentially by N_2, O, and CO. The order of retrievals is largely driven by decreasing inertness and contributions to the photoelectron flux. Since O contributes to the photoelectron flux and e + CO 4PG emission is produced solely by photoelectron impact, we retrieve O followed by CO. The retrieved density in each step of the process is included in the a priori atmosphere for the next retrieval (all other MCD 6.1 a priori species abundances not explicitly retrieved remain unchanged).

Figure 6 shows representative brightness profiles of Ar I 106.6 nm, N I 120 nm, O I 135.6 nm, and CO 4PG observed by EMUS on 1 March 2021 (SZA = 33.24°; latitude = 18.29°N; longitude = 5.55°E; L_s = 10.72°) and corresponding retrieved Ar, N_2, O, and CO densities. The EMUS observations represent the first spectrally and spatially resolved limb profiles of Ar I 106.6 nm and N I 120 nm emissions at Mars. Figure 7 shows the mean retrieved density profiles of Ar, N_2, O, and CO with 1-σ natural variability for all eight (four for Ar HR) EMUS insertion orbit profiles from 25 February 2021 to 9 March 2021. Estimated uncertainties in the EMUS observations and the a priori abundances are formally propagated to determine uncertainties in the retrieved densities. Mean uncertainties for retrieved densities over the altitude range 130–160 km are 106%, 33%, 52% and 29%, respectively, for Ar, CO, N_2, and O.

6. Discussion

While the scope of the EMUS insertion orbit special observations considered here is limited both spatially and temporally, it is worthwhile to compare our results with contemporaneous data sets and previously published

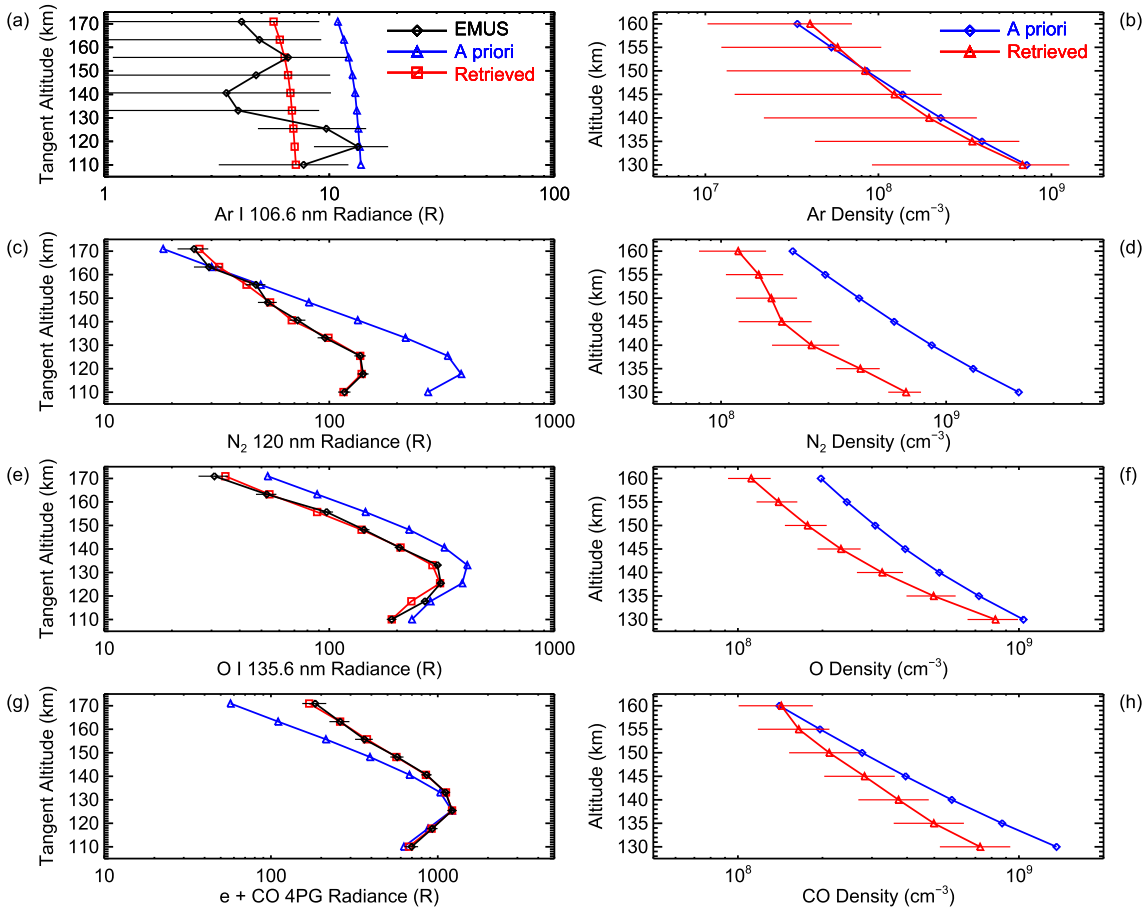

Figure 6. (a) Ar I 106.6 nm intensity profile observed by EMUS on 1 March 2021 using the HR slit (black) and best fit from optimal estimation retrieval (red). The forward model profile calculated using the a priori atmosphere is shown in blue. The black horizontal lines represent the uncertainties estimated from the multiple linear regression fit to the EMUS spectra at each tangent altitude. (b) The a priori Ar density profile used to initiate the optimal estimation retrieval (blue) and the retrieved Ar density profile (red). The red horizontal lines represent formal uncertainties estimated by the optimal estimation retrieval algorithm. (c, d) same as panels (a, b) but for N I 120 nm intensity and retrieved N_2 density. (e, f) same as panels (a, b) but for O I 135.6 nm intensity and retrieved O density. (g, h) same as panels (a, b) but for e + CO 4PG intensity and retrieved CO density.

results. Although MAVEN NGIMS measures all four of the species considered in our analysis, we note that vertical mixing ratio profiles of NGIMS CO have not been produced (Olsen et al., 2021). We compare retrieved Ar, N_2, and O densities with results reported by S. W. Stone et al. (2018), who analyzed NGIMS data for the first eight MAVEN Deep Dip campaigns and derived a correction to remove horizontal motion of the spacecraft (these corrections are not available with the operational NGIMS data products).

Mean EMUS Ar densities shown in Figure 7a are systematically lower than both MCD 6.1 and NGIMS Deep Dip 8 in situ measurements (SZA = 25.0°; L_s = 76.3°) with a mean difference of 10%–15% between 130 and 160 km. Likewise, we find that EMUS N_2 densities are systematically lower than both MCD 6.1 and NGIMS Deep Dip 8 by ~75%, whereas EMUS O densities are systematically lower by 55% and 35%, respectively (see Figures 7b and 7c). Mean retrieved N_2 and O densities from Evans et al. (2015) for the same date range as the EMUS observations (lat = 44°S; lon = 25°; SZA = 50°; LT = 13 hr) are shown in panels (b) and (c), respectively. We find that mean EMUS O densities agree with values reported by Evans et al. (2015) within respective 1-σ natural variability, whereas mean EMUS N_2 densities are systematically lower by 60%. EMUS CO densities shown in Figure 7d are lower than MCD 6.1 by 45% (S. W. Stone et al. (2018) and Evans et al. (2015) did not report CO densities).

While S. W. Stone et al. (2018) focused specifically on MAVEN Deep Dip campaigns extending down to about 125 km, Yoshida et al. (2021) utilized a larger data set comprised of nominal NGIMS measurements, albeit from higher altitudes ranging from ~150 to ~250 km. Near 160 km, Yoshida et al. (2021) report a $[N_2]/[CO_2]$ ratio of ~0.12 for L_s = 59°–63° (see their Figure 4d), which falls within the 1-σ natural variability of the mean EMUS

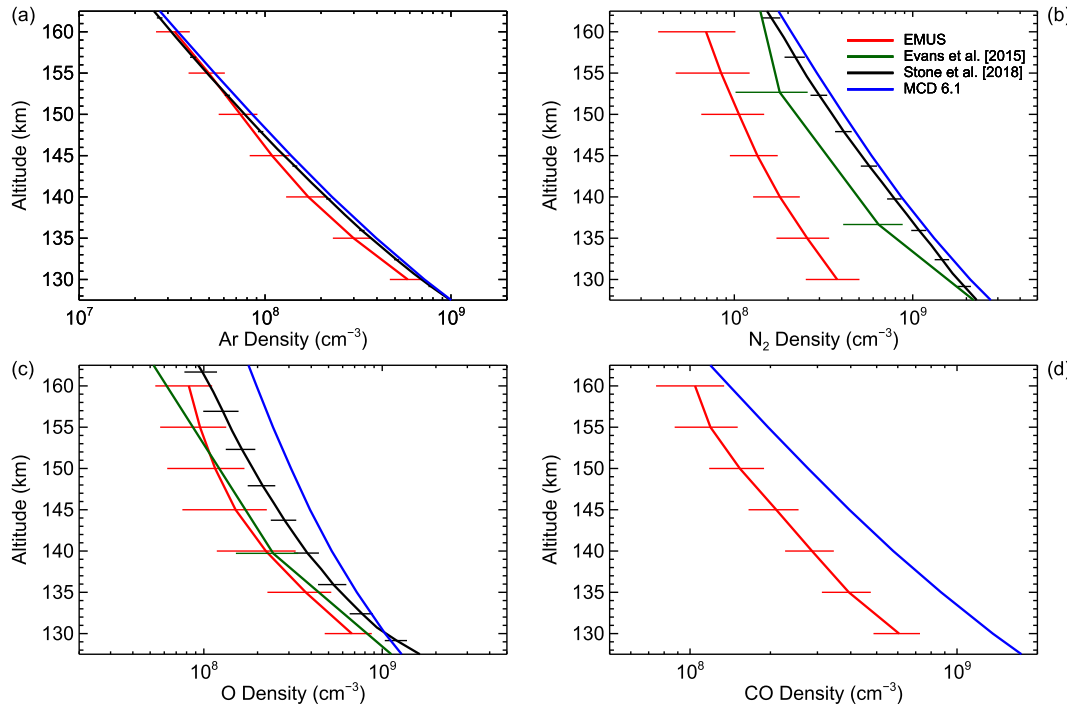

Figure 7. Mean EMUS retrieved density profiles of (a) Ar, (b) N_2, (c) O, and (d) CO are shown in red. Horizontal bars represent 1-σ natural variability of the retrieved densities. The Deep Dip 8 atm of S. W. Stone et al. (2018) is shown in black (panels a–c; L_s = 76.3°; LT = 13.7 hr; latitude = 18.9°N; SZA = 25°) with 1-σ natural variability. The mean MCD 6.1 atmosphere for the EMUS conditions (used as the a priori atmosphere for the retrievals) is shown in blue. Mean retrieved N_2 and O densities from Evans et al. (2015) for the same date range as the EMUS observations (lat = 44°S; lon = 25°; SZA = 50°; LT = 13 hr) are shown as green curves in panels (b, c), respectively, with horizontal bars representing 1-σ natural variability. Only the MCD 6.1 CO density is shown in panel (d) since Evans et al. (2015) and S. W. Stone et al. (2018) do not report CO densities.

value 0.08 ± 0.04. Similarly, Yoshida et al. (2021) (their Figure 4e) report an [O]/[CO_2] ratio of ∼0.16 near 160 km for L_s = 59°–63°, which is larger than the 1-σ natural variability of the mean EMUS value 0.10 ± 0.03.

Measurements of CO abundance in the lower atmosphere were recently made by the Atmospheric Chemistry Suite (ACS) mid-infrared channel (MIR) on board the ExoMars Trace Gas Orbiter (Olsen et al., 2021). As is the case with the EMUS observations, the ACS MIR measurements were limited and correspond to just 32 occultations recorded between L_s 164° and 220° from 24 April 2018–28 June 2018. CO number densities from the ACS MIR retrievals cover the range of 10^9–10^{10} cm^{-3} at 120 km. Neutral CO densities measured by NGIMS approach 10^{10} cm^{-3} at the lowest altitude limits of ∼130 km during MAVEN Deep Dip campaigns (Olsen et al., 2021). EMUS retrieved CO densities are therefore in qualitative agreement with ACS MIR observations and NGIMS measurements (see Figure 7d). However, a quantitative comparison is not readily attainable since the uncertainties of ACS MIR retrievals are very large above 100 km and NGIMS measurements are most reliable above 160 km (Olsen et al., 2021).

CO density profiles in the Martian atmosphere were also recently obtained for the first time from retrievals of solar occultation measurements by the Nadir and Occultation for Mars Discovery (NOMAD) onboard ExoMars TGO (Modak et al., 2023). These measurements extend to about 100 km altitude and cover L_s = 160°–354° during MY 34. The global distribution of CO abundances observed by NOMAD agrees with latitudinal and seasonal variations obtained using nadir observations (Smith et al., 2009) and with retrieved CO mixing ratios obtained from ACS observations (Olsen et al., 2021).

Figure 8 shows retrieved volume mixing ratios (VMRs) of Ar, N_2, O, and CO for all eight (four for Ar HR) EMUS insertion orbit profiles compared to MCD 6.1. Comparisons with Deep Dip 8 values from S. W. Stone et al. (2018) are shown in panels (a-c). Mean retrieved N_2 and O VMRs from Evans et al. (2015) are also shown in panels (b) and (c), respectively. The mean EMUS Ar VMR (panel a) is ∼15% higher (lower) than S. W. Stone et al. (2018) (MCD 6.1). The mean EMUS N_2 VMR is systematically lower than MCD 6.1, S. W. Stone et al. (2018), and

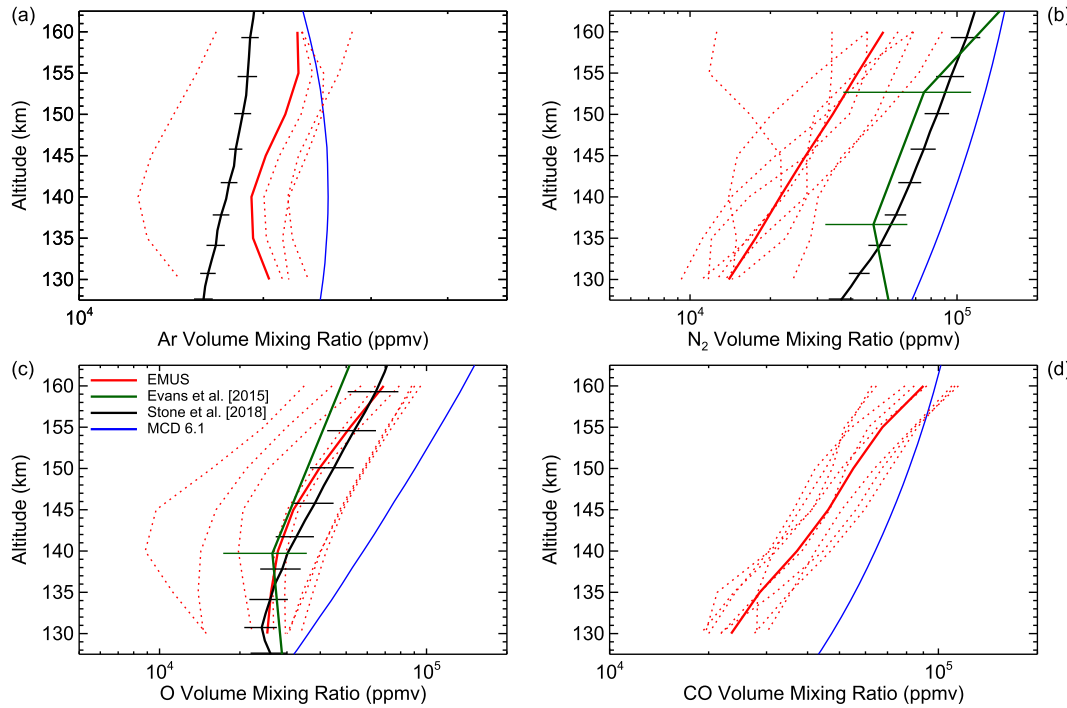

Figure 8. Retrieved volume mixing ratios (VMRs) of (a) Ar, (b) N_2, (c) O, and (d) CO for all eight (four for Ar HR) EMUS insertion orbit profiles. The mean VMR is shown as a solid red line whereas VMRs for individual EMUS profiles are shown as dotted red lines. Mean Deep Dip 8 VMRs from S. W. Stone et al. (2018) are shown in black whereas mean MCD 6.1 VMRs (i.e., the retrieval a priori atmosphere for the EMUS conditions) are shown in blue. Mean retrieved N_2 and O VMRs from Evans et al. (2015) are shown as green curves in panels (b) and (c), respectively. The horizontal bars represent 1-σ natural variability. Only the MCD 6.1 CO VMR is shown in panel (d) since Evans et al. (2015) and S. W. Stone et al. (2018) do not report CO densities.

Evans et al. (2015) by 60%–75%. The O VMR from EMUS agrees with S. W. Stone et al. (2018) and Evans et al. (2015) within respective 1-σ natural variability, but is systematically lower than MCD 6.1 by ∼50%. The mean EMUS CO VMR is lower than MCD 6.1 by 35%. If we extrapolate the mean EMUS CO VMR down to 100 km we obtain a value of $\sim 10^4$ (ppmv), which is in good qualitative agreement with CO VMRs obtained from TGO NOMAD reported by Modak et al. (2023) (their Figures 10 and 11).

7. Conclusions

We have presented the first retrievals of Ar and CO number densities in the upper atmosphere of Mars using UV dayglow observations for tangent altitudes from approximately 100 to 200 km. We use EMUS observations of Ar I 106.6 nm, N I 120 nm, and e + CO 4PG ($A - X$) for our retrievals, which are the first spectrally and spatially resolved remote sensing limb scan observations of these emissions at Mars.

Key findings from this study are:

1. Remotely sensed CO densities retrieved from 130 to 160 km for the first time agree qualitatively with TGO ACS and NOMAD and are ∼45% lower than MCD 6.1 predictions for similar conditions.
2. Mean retrieved Ar, N_2, and O densities (130–160 km), respectively, are systematically lower than MCD 6.1 and NGIMS by 10%–15%, ∼75%, and 35%–55%.
3. High spectral resolution observations by EMM EMUS show the first detection of C I 119.3 nm emission blended with N I 120 nm emission.

The EMUS high (1.3 nm) and VHR (0.4 nm) observations used in the present study provide a unique opportunity to develop and test robust spectral fitting techniques that can be used to reliably unblend UV spectra (100–190 nm) observed on the limb of Mars. While the EMUS insertion orbit special observations are limited in time and geophysical coverage, they provide important guidance for how our fitting techniques can be carefully

applied to unblend spectra of similar or lower resolution observed by other past, present, and future UV instruments. More comprehensive UV limb measurements by other missions, particularly MAVEN IUVS, can now be spectroscopically analyzed to further quantify variations of CO composition in the Martian upper atmosphere over a much wider time frame and scope of geophysical conditions.

Appendix A: CO ($C - X$) and ($E - X$) Line Lists

A1. Ab Initio Calculations

The potential energy curves and transition dipole moment curves of the CO molecule were calculated using the complete active space self-consistent field (CASSCF) method and internally contracted multireference configuration interaction (MRCI + Q) with a Davidson correction included. The calculations were conducted using the MOLPRO 2022 package (Werner et al., 2020), and the basis set used for both C and O atoms is aug-cc-pV5Z for s, p, and d functions (Pritchard et al., 2019).

Diatomic molecules belong to the $C_{\infty v}$ group, however due to MOLPRO package limitations, the $C_{\infty v}$ group was decomposed to C_{2v} symmetry. The considered active space for the CO molecules in the irreducible representation is [$6a_1$, $3b_1$, $3b_2$, $0a_2$]. This active space contains: 6σ (C: 2s, $2p_0$, 3s, $3p_0$; O: 2s, $2p_0$), 3π (C: $2p_{1\pm}$,$3p_{1\pm}$; O: $2p_{1\pm}$), 0δ orbitals. Overall, 12 molecular orbitals are considered in the active space selected to be (6,3,3,0) with (2,0,0,0) closed and core orbitals.

Figure A1 shows selected singlet potential energy curves including C $^1\Sigma^+$ and E $^1\Pi$ states that have been used in this paper and are shown here for the first time. The C $^1\Sigma^+$ state has two avoided crossings. The first one is at around 1.26 Å with D′ $^1\Sigma^+$ state, and the second one is nearby 1.48 Å with the C′ $^1\Sigma^+$ state (Lefebvre & Lewis, 2007; Vázquez et al., 2009). The C $^1\Sigma^+$ – X $^1\Sigma^+$ (0,0) and (1,0) normalized intensities were calculated over the range (0.9–1.26 Å), before the first avoided crossing.

Similarly, the E $^1\Pi$ state exhibits two avoided crossings. The first one is at around 1.32 Å with E′ $^1\Sigma^+$ state, and the second one is at around 1.58 Å with unbound $^1\Pi$ (IV) state (named here conventionally). Similar states are obtained in the literature (Lefebvre-Brion & Lewis, 2007; Vázquez et al., 2009). The E $^1\Pi$ – X $^1\Sigma^+$ (0,0) rovibrational normalized intensities were calculated over the range (0.882–1.288 Å) prior to the first avoided crossing.

The spectroscopic constants of the calculated Potential Energy Curves compare well with published literature. We consider the following parameters:

R_e: The molecule's atoms equilibrium bond distance.

T_e: The energy difference between the ground state and the excited electronic state of the diatomic molecule when the two atoms are at their equilibrium (bond) distance.

ω_e: The vibrational constant related to the curvature of the potential energy curve near its minimum. This constant provides information about the vibrational motion of the atoms in the molecule, around the equilibrium position.

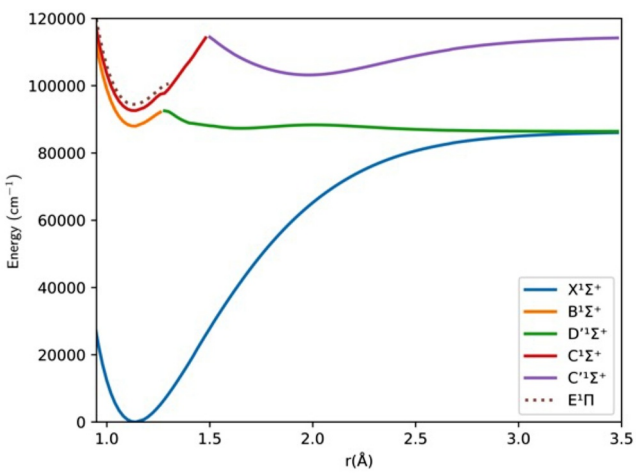

Figure A1. Selected CO singlet potential energy curves.

The values of R_e for the ground state vary between 1.13 Å and 1.14 Å according to Huber and Herzberg (1979), Peng-Fei et al. (2013), Hall et al. (1973), Cooper and Kirby (1987), Chantranupong et al. (1992), Spielfiedel et al. (1999), and Shi et al. (2013). Our calculated value for the same constant similarly tends to 1.14 Å. The same references report values for ω_e that vary as 2000.00 cm^{-1} < ω_e < 2169.81 cm^{-1}; our value (ω_e = 2125.45 cm^{-1}) agrees well with the reported values, with relative percentage difference (RD%) varying as 0.76 < ω_e (RD%) < 2.41. O'Neil and Schaefer III (1970) found that R_e = 1.24 Å and ω_e = 1854.00 cm^{-1}.

The electronic excited states C $^1\Sigma^+$ and E $^1\Pi$ also show accordance between our values and those in the literature. Eidelsberg and Rostas (1990), Eidelsberg et al. (1992), Vázquez et al. (2009), and Huber and Herzberg (1979) found that the value of R_e for the C $^1\Sigma^+$ state varies between 1.1248 Å and

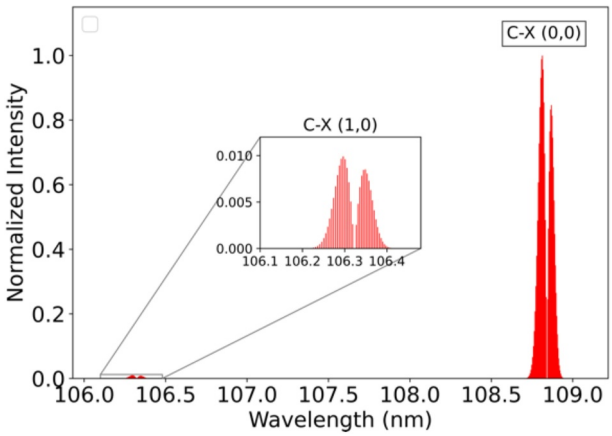

Figure A2. Simulated (0,0) band of the C $^1\Sigma^+$ – X $^1\Sigma^+$ transitions for a temperature of 200 K. The inset provides a magnified view of the (1-0) band.

1.12 Å, which is close to our obtained value of 1.13 Å. The same applies to ω_e for our calculated C $^1\Sigma^+$ state, where the value of 2119.10 cm^{-1} shows a relative percentage difference varying as $2.61 < \omega_e$ (RD%) < 3.19 with the same published papers. Similarly, the value of T_e (92,566.1 cm^{-1}) shows relative differences that vary as $0.10 < T_e$ (RD%) < 0.71 for the same C $^1\Sigma^+$ state, with the stated references.

Mainly two published works dealt with the E $^1\Pi$ state: Vázquez et al. (2009) and Huber and Herzberg (1979). Both reported a value of $R_e = 1.12$ Å for this state, while our calculations show $R_e = 1.13$ Å. Similarly, they stated values of $\omega_e = 2127.6$ cm^{-1} and 2153 cm^{-1}, in close agreement with our calculated value of $\omega_e = 2121.27$ cm^{-1}. Finally, our value of $T_e = 94{,}408.3$ cm^{-1} shows relative percentage differences of 1.62% and 1.90% with respect to the two published works.

A2. Duo/ExoCross Calculations

The program Duo (Tennyson & Yurchenko, 2017; Yurchenko et al., 2016) solves the ro-vibrational Schrödinger equation of a diatomic molecule to calculate its rotational, rovibrational, and rovibronic spectra. Its non-relativistic Hamiltonian relies on the ladder operator to couple rovibrational states that belong to different electronic states. In our case, Duo was used to calculate the rotational transitions between (C $^1\Sigma^+$ and X $^1\Sigma^+$) states and (E $^1\Pi$ and X $^1\Sigma^+$) states and generate corresponding line lists. The coupled Schrödinger equation was solved on a uniformly spaced grid of 501 points with an internuclear distance range from 0.9 to 1.25 Å using the Sinc DVR (Discrete Variable Representation) method. The ground state (X $^1\Sigma^+$) was fitted using the Extended Morse Oscillator (EMO) function and the C $^1\Sigma^+$ state using the Simons–Parr–Finlan (SPF) function (Yurchenko et al., 2016). The EMO function is given by the following equation:

$$V(r) = T_e + (A_e - T_e)\left(1 - \exp(-\beta(r)(r - r_e))\right)^2 \tag{A1}$$

where $\beta(r) = \sum_{i=0} a_i y(r)^i$, $y(r) = \left(r^p - r_e^p\right)/\left(r^p + r_e^p\right)$, T_e is the minimum electronic energy, A_e is the asymptotic limit, and r_e is the equilibrium bond length. The SPF function is given by the following equation:

$$V(r) = T_e + a_0 y^2(r)\left(1 + \sum_{i \geq 1} a_i y^i(r)\right) \tag{A2}$$

where $y(r) = (r - r_e)/r$.

The potential energy curve of the E $^1\Pi$ state was fitted to a fifth-degree polynomial. The maximum vibrational level for all three states was set to one to get the line list of the (0-0) band. The maximum energy limit was set to 110,000 cm^{-1} in our model, and the maximum rotational quantum number to 110.

ExoCross (Yurchenko et al., 2018) is a FORTRAN code that calculates absorption/emission spectra of molecules, and their corresponding cross-sections at different temperatures using line list data as input. The line intensity or the absorption coefficient (cm/molecule) is calculated using the following formula:

$$I(f \leftarrow i) = \frac{g_f^{tot} A_{fi}}{8\pi c \tilde{\nu}_{fi}^2} \frac{e^{-\frac{c_2 \tilde{E}_i}{T}}\left(1 - e^{-\frac{c_2 \tilde{\nu}_{fi}}{T}}\right)}{Q(T)} \tag{A3}$$

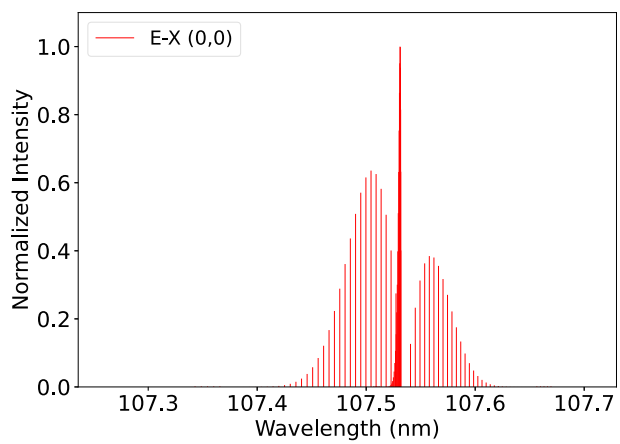

Figure A3. Simulated (0,0) band of the E $^1\Pi$ – X $^1\Sigma^+$ transitions for a temperature of 200 K.

where $\tilde{\nu}_{fi}$ is the transition wavenumber (cm^{-1}), A_{fi} is the Einstein (A) coefficient (s^{-1}), $\tilde{E}_i = E_i/hc$ is the energy term value (cm^{-1}), T is the temperature in K, c_2 is the second radiation constant ($c_2 = hc/k_B$ in cm K), and Q(T) is the partition function $\left(Q(T) = \sum_n g_n^{tot} e^{-\frac{c_2 \tilde{E}_n}{T}}\right)$, and g_n^{tot} is the total degeneracy that is a function of the nuclear-spin statistical weight factor $\left(g_n^{ns}\right)$ and rotational quantum number (J_n) $\left(g_n^{tot} = g_n^{ns}(2J_n + 1)\right)$.

Normalized simulated spectra for the (0-0) and (1-0) bands of the C $^1\Sigma^+$ – X $^1\Sigma^+$ transition are shown in Figure A2 and the normalized simulated spectrum for the (0-0) band of the E $^1\Pi$ – X $^1\Sigma^+$ transition is shown in Figure A3. The spectra were obtained using the ExoCross code at a temperature of 200 K. The spectra in Figures A2 and A3 are shown for the first time. The relative error for the C-X (0-0) band position is $0.04\% < \Delta\lambda < 0.065\%$ in comparison with Ubachs et al. (1995). For the C-X (1-0) band position, the relative error is $0.01\% < \Delta\lambda < 0.018\%$ when compared to the Federman et al. (2001). Furthermore, for the E-X (0-0) band position, the relative error is 0.065% compared to Lemaire et al. (2018). A comparison with MARVEL data using Lemaire et al. (2018), Tilford and Vanderslice (1968), and Tilford and Simmons (1972) has been conducted and it shows good agreement with our data. For the C-X (0-0) the absolute relative error is 0.02%–0.06% for all rotational levels, for the C-X (1-0) the absolute relative error is 0%–0.02% and for the E-X (0-0) the absolute relative error is 0.03%–0.07%.

Data Availability Statement

MAVEN EUVM data (Level 3; Version 15 Revision 2) are publicly available in CDF format (Eparvier, 2022). MAVEN IUVS CO_2 densities are publicly available in IDL SAV format (Evans et al., 2023b). Duo and ExoCross are freely available via https://github.com/exomol. Data from the Emirates Mars Mission (EMM) are freely and publicly available on the EMM Science Data Center (SDC, http://sdc.emiratesmarsmission.ae). This location is designated as the primary repository for all data products produced by the EMM team and is designated as long-term repository as required by the UAE Space Agency. The data available (http://sdc.emiratesmarsmission.ae/data) include ancillary spacecraft data, instrument telemetry, Level 1 (raw instrument data) to Level 3 (derived science products), quicklook products, and data users guides to assist in the analysis of the data (https://sdc.emiratesmarsmission.ae/documentation). Following the creation of a free login, all EMM data are searchable via parameters such as product file name, solar longitude, acquisition time, sub-spacecraft latitude and longitude, instrument, data product level, etc.

Data products can be browsed within the EMM SDC via a standardized file system structure that follows the convention:

/emm/data/<Instrument>/<DataLevel>/<Mode/<Year>/<Month>

Data product filenames follow a standard convention:

emm_<Instrument>_<DataLevel><StartTimeUTC>_<OrbitNumber>_<Mode>_

<Description>_<KernelLevel>_<Version>. <FileType>

Emirates Mars Ultraviolet Spectrograph (EMUS; Holsclaw et al., 2021) data and users guides are available at: https://sdc.emiratesmarsmission.ae/data/emus.

Radiances, densities, and corresponding uncertainties utilized in the present analysis can be obtained from Evans et al. (2024).

Acknowledgments
Funding for development of the Emirates Mars mission was provided by the UAE government. NEK is funded by the ASPIRE Award for Research Excellence (AARE20-000329-00001) and is partially supported by the Space and Planetary Science Center at Khalifa University through the award 8474000336-KU-SPSC. NEK also acknowledges the use of Khalifa University Almesbar HPC. JT and SNY thank the European Research Council (ERC) for funding under the European Union's Horizon 2020 research and innovation programme through Advance Grant 883830. The authors acknowledge significant contributions by the late Samuel Durrance in advancing our understanding of the CO 4PG ($A - X$) band system. Durrance's seminal work published over 40 years ago made the present analysis possible. The authors thank Shane Stone for providing MAVEN Deep Dip 8 NGIMS densities.

References

Ajello, J. (1971). Emission cross sections of CO_2 by electron impact in the interval 1260–4500 Å. II. *The Journal of Chemical Physics*, *55*(7), 3169–3177. https://doi.org/10.1063/1.1676564

Ajello, J., & Shemansky, D. (1985). A reexamination of important N2 cross sections by electron impact with application to the dayglow: The Lyman-Birge-Hopfield Band System and NI (119.99 nm). *Journal of Geophysical Research*, *90*(A10), 9845–9861. https://doi.org/10.1029/ja090ia10p09845

Ajello, J. M., Malone, C. P., Evans, J. S., Holsclaw, G. M., Hoskins, A. C., Jain, S. K., et al. (2019). UV study of the Fourth Positive Band System of CO and O I 135.6 nm from electron impact on CO and CO_2. *Journal of Geophysical Research (Space Physics)*, *124*(4), 2954–2977. https://doi.org/10.1029/2018JA026308

Al Matroushi, H., Al Mazmi, H., Al Mheiri, N., Al Shamsi, M., Al Tunaiji, E., Badri, K., et al. (2021). Emirates Mars mission characterization of Mars atmosphere dynamics and processes. *Space Science Reviews*, *217*(8), 89. https://doi.org/10.1007/s11214-021-00851-6

Amiri, H., Brain, D., Sharaf, O., Withnell, P., McGrath, M., Alloghani, M., et al. (2022). The emirates Mars mission. *Space Science Reviews*, *218*(1), 1–46. https://doi.org/10.1007/s11214-021-00868-x

Barth, C., Fastie, W., Hord, C., Pearce, J., Kelly, K., Stewart, A., et al. (1969). Mariner 6: Ultraviolet spectrum of Mars upper atmosphere. *Science*, *165*(3897), 1004–1005. https://doi.org/10.1126/science.165.3897.1004

Barth, C., Hord, C., Pearce, J., Kelly, K., Anderson, G., & Stewart, A. (1971). Mariner 6 and 7 ultraviolet spectrometer experiment: Upper atmosphere data. *Journal of Geophysical Research*, *76*(10), 2213–2227. https://doi.org/10.1029/ja076i010p02213

Barth, C., Stewart, A., Hord, C., & Lane, A. (1972). Mariner 9 ultraviolet spectrometer experiment: Mars airglow spectroscopy and variations in Lyman alpha. *Icarus*, *17*(2), 457–468. https://doi.org/10.1016/0019-1035(72)90011-5

Bertaux, J.-L., Leblanc, F., Perrier, S., Quémerais, E., Korablev, O., Dimarellis, E., et al. (2005a). Nightglow in the upper atmosphere of Mars and implications for atmospheric transport. *Science*, *307*(5709), 566–569. https://doi.org/10.1126/science.1106957

Bertaux, J.-L., Leblanc, F., Perrier, S., Quemerais, E., Korablev, O., Forget, F., et al. (2005b). Detection of Martian nightglow: NO recombination bands and aurora over crustal magnetic anomalies. *AGU Fall Meeting Abstracts*, *2005*, P14A-P07.

Bertaux, J.-L., Leblanc, F., Witasse, O., Quemerais, E., Lilensten, J., Stern, S., et al. (2005c). Discovery of an aurora on Mars. *Nature*, *435*(7043), 790–794. https://doi.org/10.1038/nature03603

Bishop, J., & Feldman, P. D. (2003). Analysis of the Astro-1/Hopkins Ultraviolet Telescope EUV–FUV dayside nadir spectral radiance measurements. *Journal of Geophysical Research*, *108*(A6). https://doi.org/10.1029/2001ja000330

Bishop, J., Stevens, M. H., & Feldman, P. D. (2007). Molecular nitrogen Carroll-Yoshino v' = 0 emission in the thermospheric dayglow as seen by the Far Ultraviolet Spectroscopic Explorer. *Journal of Geophysical Research*, *112*(A10). https://doi.org/10.1029/2007ja012389

Bougher, S., Jakosky, B., Halekas, J., Grebowsky, J., Luhmann, J., Mahaffy, P., et al. (2015). Early MAVEN deep dip campaign reveals thermosphere and ionosphere variability. *Science*, *350*(6261), aad0459. https://doi.org/10.1126/science.aad0459

Brain, D., Halekas, J., Peticolas, L., Lin, R., Luhmann, J., Mitchell, D., et al. (2006). On the origin of aurorae on Mars. *Geophysical Research Letters*, *33*(1). https://doi.org/10.1029/2005gl024782

Budzien, S., Feldman, P., & Conway, R. (1994). Observations of the far ultraviolet airglow by the ultraviolet limb imaging experiment on STS-39. *Journal of Geophysical Research*, *99*(A12), 23275–23287. https://doi.org/10.1029/94ja01543

Carnall, A. C. (2017). SpectRes: A fast spectral resampling tool in Python. *arXiv e-prints, arXiv:1705.05165*.

Chaffin, M. S., Deighan, J., Jain, S., Holsclaw, G., AlMazmi, H., Chirakkil, K., et al. (2022). Combined analysis of hydrogen and oxygen 102.6 nm emission at Mars. *Geophysical Research Letters*, *49*(16), e2022GL099851. https://doi.org/10.1029/2022gl099851

Chantranupong, L., Bhanuprakash, K., Honigmann, M., Hirsch, G., & Buenker, R. J. (1992). A configuration interaction study of the oscillator strengths for various low-lying transitions of the CO molecule. *Chemical Physics*, *161*(3), 351–362. https://doi.org/10.1016/0301-0104(92)80152-l

Cooper, D. L., & Kirby, K. (1987). Theoretical study of low-lying $1\sigma+$ and 1π states of co. I. potential energy curves and dipole moments. *The Journal of Chemical Physics*, *87*(1), 424–432. https://doi.org/10.1063/1.453587

Cox, C., Saglam, A., Gérard, J.-C., Bertaux, J.-L., González-Galindo, F., Leblanc, F., & Reberac, A. (2008). Distribution of the ultraviolet nitric oxide Martian night airglow: Observations from Mars express and comparisons with a one-dimensional model. *Journal of Geophysical Research*, *113*(E8). https://doi.org/10.1029/2007je003037

Dubinin, E., Fraenz, M., Woch, J., Barabash, S., & Lundin, R. (2009). Long-lived auroral structures and atmospheric losses through auroral flux tubes on Mars. *Geophysical Research Letters*, *36*(8). https://doi.org/10.1029/2009gl038209

Durrance, S. T. (1981). The carbon monoxide fourth positive bands in the Venus dayglow 1. Synthetic spectra. *Journal of Geophysical Research*, *86*(A11), 9115–9124. https://doi.org/10.1029/ja086ia11p09115

Eidelsberg, M., Benayoun, J., Viala, Y., Rostas, F., Smith, P., Yoshino, K., et al. (1992). Recalibration of the absorption/photodissociation spectra of CO and its isotopes between 91 and 115 nm. *Astronomy and Astrophysics*, *265*(2), 839–842.

Eidelsberg, M., & Rostas, F. (1990). Spectroscopic, absorption and photodissociation data for CO and isotopic species between 91 and 115 nm. *Astronomy and Astrophysics*, *235*, 472–489.

Eparvier, F. G. (2022). MAVEN EUV modelled data bundle [Dataset]. *NASA Planetary Data System*. https://doi.org/10.17189/1517691

Evans, J., Correira, J., Deighan, J., Jain, S., Al Matroushi, H., Al Mazmi, H., et al. (2022). Retrieval of CO relative column abundance in the Martian thermosphere from FUV disk observations by EMM EMUS. *Geophysical Research Letters*, *49*(18), e2022GL099615. https://doi.org/10.1029/2022gl099615

Evans, J., Soto, E., Jain, S., Deighan, J., Stevens, M., Chaffin, M., et al. (2023a). Dayside temperature maps of the upper mesosphere and lower thermosphere of Mars retrieved from MAVEN IUVS observations of OI 297.2 nm emission. *Journal of Geophysical Research: Planets*, *128*(2), e2022JE007325. https://doi.org/10.1029/2022je007325

Evans, J., Soto, E., Jain, S. K., Deighan, J., Stevens, M. H., Chaffin, M. S., et al. (2023b). Dayside temperature maps of the upper mesosphere and lower thermosphere of Mars retrieved from MAVEN IUVS observations of O I 297.2 nm emission [Dataset]. *University of Colorado Boulder*, *128*(2). https://doi.org/10.25810/1BKN-BS85

Evans, J. S., Deighan, J., Jain, S., Veibell, V., Correira, J., Al Matroushi, H., et al. (2024). Retrieval of Ar, N_2, O, and CO in the Martian thermosphere using dayglow limb observations by EMM EMUS [Dataset]. https://doi.org/10.5061/dryad.dv41ns253

Evans, J. S., Stevens, M. H., Lumpe, J. D., Schneider, N. M., Stewart, A. I. F., Deighan, J., et al. (2015). Retrieval of CO_2 and N_2 in the Martian thermosphere using dayglow observations by IUVS on MAVEN. *Geophysical Research Letters*, *42*(21), 9040–9049. https://doi.org/10.1002/2015GL065489

Federman, S., Fritts, M., Cheng, S., Menningen, K., Knauth, D. C., & Fulk, K. (2001). Oscillator strengths for BX, CX, and EX transitions in carbon monoxide. *The Astrophysical Journal - Supplement Series*, *134*(1), 133–138. https://doi.org/10.1086/320361

Feldman, P. D., Burgh, E. B., Durrance, S. T., & Davidsen, A. F. (2000). Far-ultraviolet spectroscopy of Venus and Mars at 4 Å resolution with the Hopkins ultraviolet telescope on Astro-2. *The Astrophysical Journal*, *538*(1), 395–400. https://doi.org/10.1086/309125

Fox, J. L. (1992). Airglow and aurora in the atmospheres of Venus and Mars. *Washington DC American Geophysical Union Geophysical Monograph Series*, *66*, 191–222. https://doi.org/10.1029/gm066p0191

Fox, J. L., & Dalgarno, A. (1979). Ionization, luminosity, and heating of the upper atmosphere of Mars. *Journal of Geophysical Research*, *84*(A12), 7315–7333. https://doi.org/10.1029/JA084iA12p07315

Fox, J. L., & Hać, A. B. (2018). Escape of O (3P), O (1D), and O (1S) from the Martian atmosphere. *Icarus*, *300*, 411–439. https://doi.org/10.1016/j.icarus.2017.08.041

Gladstone, G. R. (1982). Radiative transfer with partial frequency redistribution in inhomogeneous atmospheres: Application to the Jovian aurora. *Journal of Quantitative Spectroscopy and Radiative Transfer*, *27*(5), 545–556. https://doi.org/10.1016/0022-4073(82)90107-8

Hall, J., Schamps, J., Robbe, J., & Lefebvre-Brion, H. (1973). Theoretical study of the perturbation parameters in the a 3π and a 1π states of co. *The Journal of Chemical Physics*, *59*(6), 3271–3283. https://doi.org/10.1063/1.1680469

Holsclaw, G. M., Deighan, J., Almatroushi, H., Chaffin, M., Correira, J., Evans, J. S., et al. (2021). The emirates Mars ultraviolet spectrometer (EMUS) for the EMM mission. *Space Science Reviews*, *217*(8), 1–49. https://doi.org/10.1007/s11214-021-00854-3

Huber, K., & Herzberg, G. (1979). *Molecular spectra and molecular structure IV. Constants of diatomic molecules*. Springer Science & Business Media.

Huestis, D. L., & Berkowitz, J. (2011). Critical evaluation of the photoabsorption cross section of CO_2 from 0.125 to 201.6 nm at room temperature. In *Advances in geosciences: Volume 25: Planetary science (PS)* (pp. 229–242). World Scientific.

Ip, W.-H. (2012). Ena diagnostics of auroral activity at Mars. *Planetary and Space Science*, *63*, 83–86. https://doi.org/10.1016/j.pss.2011.10.009

Jackman, C., Garvey, R., & Green, A. (1977). Electron impact on atmospheric gases, I. updated cross sections. *Journal of Geophysical Research*, *82*(32), 5081–5090. https://doi.org/10.1029/ja082i032p05081

Jain, S. K., Bougher, S. W., Deighan, J., Schneider, N. M., González Galindo, F., Stewart, A. I. F., et al. (2020). Martian thermospheric warming associated with the planet encircling dust event of 2018. *Geophysical Research Letters*, *47*(3), e85302. https://doi.org/10.1029/2019GL085302

Jain, S. K., Stewart, A. I. F., Schneider, N. M., Deighan, J., Stiepen, A., Evans, J. S., et al. (2015). The structure and variability of Mars upper atmosphere as seen in MAVEN/IUVS dayglow observations. *Geophysical Research Letters*, *42*(21), 9023–9030. https://doi.org/10.1002/2015GL065419

Jakosky, B. M., Lin, R. P., Grebowsky, J. M., Luhmann, J. G., Mitchell, D., Beutelschies, G., et al. (2015). The Mars atmosphere and volatile evolution (MAVEN) mission. *Space Science Reviews*, *195*(1), 3–48. https://doi.org/10.1007/s11214-015-0139-x

Kassal, T. T. (1975). Resonant fluorescent scattering of solar radiation by the fourth positive band system of CO. *Applied Optics*, *14*(7), 1513–1515. https://doi.org/10.1364/ao.14.001513

Kassal, T. T. (1976). Scattering of solar Lyman alpha by the (14, 0) band of the fourth positive system of CO. *Journal of Geophysical Research*, *81*(7), 1411–1412. https://doi.org/10.1029/ja081i007p01411

Krasnopolsky, V. A., & Feldman, P. D. (2002). Far ultraviolet spectrum of Mars. *Icarus*, *160*(1), 86–94. https://doi.org/10.1006/icar.2002.6949

Leblanc, F., Witasse, O., Lilensten, J., Frahm, R., Safaenili, A., Brain, D., et al. (2008). Observations of aurorae by SPICAM ultraviolet spectrograph on board Mars express: Simultaneous ASPERA-3 and MARSIS measurements. *Journal of Geophysical Research*, *113*(A8). https://doi.org/10.1029/2008ja013033

Leblanc, F., Witasse, O., Winningham, J., Brain, D., Lilensten, J., Blelly, P.-L., et al. (2006). Origins of the Martian aurora observed by spectroscopy for investigation of characteristics of the atmosphere of Mars (SPICAM) on board Mars express. *Journal of Geophysical Research*, *111*(A9). https://doi.org/10.1029/2006ja011763

Lefebvre-Brion, H., & Lewis, B. (2007). Comparison between predissociation mechanisms in two isoelectronic molecules: CO and N2. *Molecular Physics*, *105*(11–12), 1625–1630. https://doi.org/10.1080/00268970701390180

Lemaire, J.-L., Heays, A., Eidelsberg, M., Gavilan, L., Stark, G., Federman, S., et al. (2018). Atlas of new and revised high-resolution spectroscopy of six CO isotopologues in the 101–115 nm range-transition energies of the v'= 0, 1, 2, and 3 to v"= 0 bands of the b1σ+, c1σ+, and e1π to x1σ+ states, related term values, and molecular constants. *Astronomy & Astrophysics*, *614*, A114. https://doi.org/10.1051/0004-6361/201732114

Lootah, F. H., Deighan, J., Fillingim, M., Jain, S., Evans, J. S., Al Matroushi, H., et al. (2022). Emirates Mars ultraviolet spectrometer's (EMUS) observation of argon in the Martian thermosphere. *Geophysical Research Letters*, *49*(17), e2022GL099852. https://doi.org/10.1029/2022gl099852

Lumpe, J. D., Bevilacqua, R. M., Hoppel, K. W., Krigman, S. S., Kriebel, D. L., Debrestian, D. J., et al. (1997). POAM II retrieval algorithm and error analysis. *Journal of Geophysical Research*, *102*(D19), 23593–23614. https://doi.org/10.1029/97JD00906

Lumpe, J. D., Bevilacqua, R. M., Hoppel, K. W., & Randall, C. E. (2002). POAM III retrieval algorithm and error analysis. *Journal of Geophysical Research (Atmospheres)*, *107*(D21), 4575. https://doi.org/10.1029/2002JD002137

Lumpe, J. D., Floyd, L. E., Herring, L. C., Gibson, S. T., & Lewis, B. R. (2007). Measurements of thermospheric molecular oxygen from the solar ultraviolet spectral irradiance monitor. *Journal of Geophysical Research (Atmospheres)*, *112*(D16), 16308. https://doi.org/10.1029/2006JD008076

Mahaffy, P. R., Benna, M., Elrod, M., Yelle, R. V., Bougher, S. W., Stone, S. W., & Jakosky, B. M. (2015). Structure and composition of the neutral upper atmosphere of Mars from the MAVEN NGIMS investigation. *Geophysical Research Letters*, *42*(21), 8951–8957. https://doi.org/10.1002/2015gl065329

McClintock, W. E., Schneider, N. M., Holsclaw, G. M., Clarke, J. T., Hoskins, A. C., Stewart, I., et al. (2015). The imaging ultraviolet spectrograph (IUVS) for the MAVEN mission. *Space Science Reviews*, *195*(1–4), 75–124. https://doi.org/10.1007/s11214-014-0098-7

Meier, R. (1991). Ultraviolet spectroscopy and remote sensing of the upper atmosphere. *Space Science Reviews*, *58*(1), 1–185. https://doi.org/10.1007/bf01206000

Millour, E., Forget, F., Spiga, A., Vals, M., Zakharov, V., & Montabone, L. (2018). Mars climate database. From Mars Express to ExoMars, *68*.

Modak, A., López-Valverde, M. A., Brines, A., Stolzenbach, A., Funke, B., González-Galindo, F., et al. (2023). Retrieval of Martian atmospheric CO vertical profiles from NOMAD observations during the first year of TGO operations. *Journal of Geophysical Research: Planets*, *128*(3), e2022JE007282. https://doi.org/10.1029/2022je007282

Olsen, K., Lefèvre, F., Montmessin, F., Fedorova, A., Trokhimovskiy, A., Baggio, L., et al. (2021). The vertical structure of CO in the Martian atmosphere from the ExoMars trace gas orbiter. *Nature Geoscience*, *14*(2), 67–71. https://doi.org/10.1038/s41561-020-00678-w

O'Neil, S. V., & Schaefer, H. F., III. (1970). Valence-excited states of carbon monoxide. *The Journal of Chemical Physics*, *53*(10), 3994–4004. https://doi.org/10.1063/1.1673871

Ott, U. (1991). Composition of the Martian atmosphere. *Space Science Reviews*, *56*(1), 23–29. https://doi.org/10.1007/bf00178387

Peng-Fei, L., Lei, Y., Zhong-Yuan, Y., Yu-Feng, G., & Tao, G. (2013). An accurate calculation of potential energy curves and transition dipole moment for low-lying electronic states of CO. *Communications in Theoretical Physics*, *59*(2), 193–198. https://doi.org/10.1088/0253-6102/59/2/11

Perrier, S., Bertaux, J.-L., Lefèvre, F., Lebonnois, S., Korablev, O., Fedorova, A., & Montmessin, F. (2006). Global distribution of total ozone on Mars from SPICAM/MEX UV measurements. *Journal of Geophysical Research*, *111*(E9). https://doi.org/10.1029/2006je002681

Peterson, W., Thiemann, E. B., Eparvier, F. G., Andersson, L., Fowler, C., Larson, D., et al. (2016). Photoelectrons and solar ionizing radiation at Mars: Predictions versus MAVEN observations. *Journal of Geophysical Research: Space Physics*, *121*(9), 8859–8870. https://doi.org/10.1002/2016ja022677

Pritchard, B. P., Altarawy, D., Didier, B., Gibson, T. D., & Windus, T. L. (2019). New basis set exchange: An open, up-to-date resource for the molecular sciences community. *Journal of Chemical Information and Modeling*, *59*(11), 4814–4820. https://doi.org/10.1021/acs.jcim.9b00725

Schindhelm, E., Stern, S. A., Gladstone, R., & Zangari, A. (2015). Pluto and Charon's UV spectra from IUE to new horizons. *Icarus*, *246*, 206–212. https://doi.org/10.1016/j.icarus.2014.03.003

Shi, D.-H., Li, W.-T., Sun, J.-F., & Zhu, Z.-L. (2013). Theoretical study of spectroscopic and molecular properties of several low-lying electronic states of CO molecule. *International Journal of Quantum Chemistry*, *113*(7), 934–942. https://doi.org/10.1002/qua.24036

Simon, C., Witasse, O., Leblanc, F., Gronoff, G., & Bertaux, J. L. (2009). Dayglow on Mars: Kinetic modelling with SPICAM UV limb data. *Planetary and Space Science*, *57*(8–9), 1008–1021. https://doi.org/10.1016/j.pss.2008.08.012

Smith, M. D., Wolff, M. J., Clancy, R. T., & Murchie, S. L. (2009). Compact reconnaissance imaging spectrometer observations of water vapor and carbon monoxide. *Journal of Geophysical Research*, *114*(E2). https://doi.org/10.1029/2008je003288

Spielfiedel, A., Tchang-Brillet, W., Dayou, F., & Feautrier, N. (1999). Ab initio calculation of the dipole transition moment and band oscillator strengths of the CO (AX) transition. *Astronomy and Astrophysics*, *346*, 699–704.

Steffl, A. J., Young, L. A., Strobel, D. F., Kammer, J. A., Evans, J. S., Stevens, M. H., et al. (2020). Pluto's ultraviolet spectrum, surface reflectance, and airglow emissions. *The Astronomical Journal*, *159*(6), 274. https://doi.org/10.3847/1538-3881/ab8d1c

Stevens, M. H., Evans, J. S., Lumpe, J., Westlake, J. H., Ajello, J. M., Bradley, E. T., & Esposito, L. W. (2015). Molecular nitrogen and methane density retrievals from Cassini UVIS dayglow observations of Titan's upper atmosphere. *Icarus*, *247*, 301–312. https://doi.org/10.1016/j.icarus.2014.10.008

Stevens, M. H., Evans, J. S., Schneider, N. M., Stewart, A. I. F., Deighan, J., Jain, S. K., et al. (2015). New observations of molecular nitrogen in the Martian upper atmosphere by IUVS on MAVEN. *Geophysical Research Letters*, *42*(21), 9050–9056. https://doi.org/10.1002/2015GL065319

Stevens, M. H., Siskind, D. E., Evans, J. S., Jain, S. K., Schneider, N. M., Deighan, J., et al. (2017). Martian mesospheric cloud observations by IUVS on MAVEN: Thermal tides coupled to the upper atmosphere. *Geophysical Research Letters*, *44*(10), 4709–4715. https://doi.org/10.1002/2017GL072717

Stewart, A. (1972). Mariner 6 and 7 ultraviolet spectrometer experiment: Implications of CO_2+, CO and O airglow. *Journal of Geophysical Research*, *77*(1), 54–68. https://doi.org/10.1029/ja077i001p00054

Stewart, A., Barth, C., Hord, C., & Lane, A. (1972). Mariner 9 ultraviolet spectrometer experiment: Structure of Mars' upper atmosphere. *Icarus*, *17*(2), 469–474. https://doi.org/10.1016/0019-1035(72)90012-7

Stone, E., & Zipf, E. (1973). Excitation of atomic nitrogen by electron impact. *The Journal of Chemical Physics*, *58*(10), 4278–4284. https://doi.org/10.1063/1.1678984

Stone, S. W., Yelle, R. V., Benna, M., Elrod, M. K., & Mahaffy, P. R. (2018). Thermal structure of the Martian upper atmosphere from MAVEN NGIMS. *Journal of Geophysical Research: Planets*, *123*(11), 2842–2867. https://doi.org/10.1029/2018je005559

Strickland, D., Bishop, J., Evans, J., Majeed, T., Shen, P., Cox, R., et al. (1999). Atmospheric Ultraviolet Radiance Integrated Code (AURIC): Theory, software architecture, inputs, and selected results. *Journal of Quantitative Spectroscopy and Radiative Transfer*, *62*(6), 689–742. https://doi.org/10.1016/s0022-4073(98)00098-3

Strickland, D., Stewart, A., Barth, C., Hord, C., & Lane, A. (1973). Mariner 9 ultraviolet spectrometer experiment: Mars atomic oxygen 1304-A emission. *Journal of Geophysical Research*, *78*(22), 4547–4559. https://doi.org/10.1029/ja078i022p04547

Strickland, D., Thomas, G., & Sparks, P. (1972). Mariner 6 and 7 ultraviolet spectrometer experiment: Analysis of the OI 1304-and 1356-A emissions. *Journal of Geophysical Research*, *77*(22), 4052–4068. https://doi.org/10.1029/ja077i022p04052

Strobel, D. F., Meier, R., Summers, M. E., & Strickland, D. J. (1991). Nitrogen airglow sources: Comparison of Triton, Titan, and Earth. *Geophysical Research Letters*, *18*(4), 689–692. https://doi.org/10.1029/91gl00133

Strobel, D. F., Summers, M. E., & Zhu, X. (1992). Titan's upper atmosphere: Structure and ultraviolet emissions. *Icarus*, *100*(2), 512–526. https://doi.org/10.1016/0019-1035(92)90114-m

Tennyson, J., & Yurchenko, S. N. (2017). The ExoMol project: Software for computing large molecular line lists. *International Journal of Quantum Chemistry*, *117*(2), 92–103. https://doi.org/10.1002/qua.25190

Tilford, S., & Simmons, J. (1972). Atlas of the observed absorption spectrum of carbon monoxide between 1060 and 1900 Å. *Journal of Physical and Chemical Reference Data*, *1*(1), 147–188. https://doi.org/10.1063/1.3253097

Tilford, S., & Vanderslice, J. T. (1968). High resolution vacuum ultraviolet absorption spectra of the b 1 σ+-x 1 σ+, c 1 σ+-x 1 σ+, and i 3 σ+-x 1 σ+ transitions in carbon monoxide. *Journal of Molecular Spectroscopy*, *26*(4), 419–431. https://doi.org/10.1016/s0022-2852(68)80056-6

Tilford, S., Vanderslice, J. T., & Wilkinson, P. (1965). High-resolution vacuum ultraviolet absorption spectrum of the e 1π ← x 1σ+ transition in CO. *Canadian Journal of Physics*, *43*(3), 450–456. https://doi.org/10.1139/p65-042

Tsurubuchi, S., Miyazaki, T., & Motohashi, K. (1996). Electron-impact emission cross sections of Ar. *Journal of Physics. B, Atomic, Molecular and Optical Physics*, *29*.

Ubachs, W., Hinnen, P., Hansen, P., Stolte, S., Hogervorst, W., & Cacciani, P. (1995). Laser spectroscopic studies of thec1σ+, v = 0 andv = 1 states of CO. *Journal of Molecular Spectroscopy*, *174*(2), 388–396. https://doi.org/10.1006/jmsp.1995.0010

Vázquez, G., Amero, J., Liebermann, H., & Lefebvre-Brion, H. (2009). Potential energy curves for the 1σ+ and 1, 3π states of CO. *The Journal of Physical Chemistry A*, *113*(47), 13395–13401. https://doi.org/10.1021/jp902730d

Venot, O., Bénilan, Y., Fray, N., Gazeau, M.-C., Lefèvre, F., Es-sebbar, E., et al. (2018). VUV-absorption cross section of carbon dioxide from 150 to 800 K and applications to warm exoplanetary atmospheres. *Astronomy & Astrophysics*, *609*, A34. https://doi.org/10.1051/0004-6361/201731295

Virtanen, P., Gommers, R., Oliphant, T. E., Haberland, M., Reddy, T., Cournapeau, D., et al., SciPy 1.0 Contributors. (2020). SciPy 1.0: Fundamental algorithms for scientific computing in Python. *Nature Methods*, *17*(3), 261–272. https://doi.org/10.1038/s41592-019-0686-2

Werner, H.-J., Knowles, P. J., Manby, F. R., Black, J. A., Doll, K., Heßelmann, A., et al. (2020). The Molpro quantum chemistry package. *The Journal of Chemical Physics*, *152*(14), 144107. https://doi.org/10.1063/5.0005081

Yoshida, N., Terada, N., Nakagawa, H., Brain, D. A., Sakai, S., Nakamura, Y., et al. (2021). Seasonal and dust-related variations in the dayside thermospheric and ionospheric compositions of Mars observed by MAVEN/NGIMS. *Journal of Geophysical Research: Planets*, *126*(11), e2021JE006926. https://doi.org/10.1029/2021je006926

Yurchenko, S. N., Al-Refaie, A. F., & Tennyson, J. (2018). Exocross: A general program for generating spectra from molecular line lists. *Astronomy & Astrophysics*, *614*, A131. https://doi.org/10.1051/0004-6361/201732531

Yurchenko, S. N., Lodi, L., Tennyson, J., & Stolyarov, A. V. (2016). Duo: A general program for calculating spectra of diatomic molecules. *Computer Physics Communications*, *202*, 262–275. https://doi.org/10.1016/j.cpc.2015.12.021